RSC Advances

PAPER

View Article Online
View Journal | View Issue

Cite this: *RSC Adv.*, 2026, **16**, 25892

Zn(II)-based metal–organic frameworks with tailored architectures: optimizing fluorescence performance for cell imaging and cancer therapy

Jinglu Wang,†[a] Yutong Chen,†[b] Danian Tian,*[a] Siyi Li,[b] Peipei Cen *[a] and Xiangyu Liu [b]

Metal–organic frameworks (MOFs) show great potential in bioimaging and cancer therapy owing to their tunable structures and unique photophysical properties. Here, based on the modulation of reactant loads and autoclave loading level, two Zn(II)-containing MOFs with the formula $C_{22}H_{18}N_4O_6Zn$ (**1**) and $C_{22}H_{18}N_4O_6Zn$ (**2**) are synthesized with 2,5-dihydroxyterephthalic acid (DHTA) and 1,4-bis((1*H*-imidazol-1-yl)methyl)benzene (bix) ligands. Structurally, **1** forms a 3D supramolecular network constructed by π–π stacking between 2D layers, while **2** is indicative of an interpenetrated 3D framework, where the Zn(II) center exhibits a more ideal tetrahedral coordination geometry. In ultrapure water, both compounds exhibit intense green fluorescence, originating from ligand-centered charge-transfer transitions, with compound **2** demonstrating superior photochemical properties (E_{m1} = 530 nm and E_{m2} = 522 nm). Compound **2** possesses a markedly higher fluorescence quantum yield (Φ = 13.78%) compared to compound **1** (Φ = 6.02%), and the average lifetimes for **1** and **2** are 0.83 and 0.98 μs, respectively. Moreover, both MOFs maintain robust fluorescence stability against diverse biological cations and anions, with **2** showing relatively high emission intensity across all ionic conditions. Biologically, **1** exhibits potent cytotoxicity against HeLa cells *via* co-activating apoptosis, ferroptosis, endoplasmic reticulum stress, and autophagy, while **2** is highly biocompatible with HeLa cells and exhibits cell-type-adaptive subcellular localization, enabling the clear imaging of the HeLa, SH-SY5Y, and A549 cells. Notably, both compounds show concentration-dependent dual functionality in the SH-SY5Y cells: low concentrations enable fluorescence imaging, while high concentrations inhibit cell proliferation. The structure–function relationship is also explored.

Received 12th March 2026
Accepted 13th April 2026

DOI: 10.1039/d6ra02099b

rsc.li/rsc-advances

Introduction

Metal–organic frameworks (MOFs) have emerged as versatile materials in bioimaging and cancer therapy due to their tunable structures, high biocompatibility, and unique photophysical properties.[1] Among them, Zn(II)-based MOFs are particularly attractive for fluorescent bioapplications, as the d^{10} electronic configuration of Zn(II) ions minimizes non-radiative electron relaxation, enabling efficient ligand-centered fluorescence emission.[2] Additionally, Zn typically forms four- to six-coordinate complexes with high coordination flexibility, allowing simultaneous binding to carboxylate and imidazole groups for the construction of multidimensional networks. Notably, the mixed-ligand strategy (combining carboxylate and imidazole ligands) facilitates the formation of high-dimensional MOF structures, which significantly enhance their stability in aqueous and organic solvent environments, an essential prerequisite for applications in humid or complex biological systems. Despite these advantages, the rational design of Zn(II)-MOFs with tailored frameworks and coordination geometries holds great promise for optimizing their luminescent performance and biological functionalities, yet subtle structural modifications induced by synthesis conditions often lead to significant differences in properties, which remain to be systematically explored.

Fluorescent probes for cancer cell imaging require not only intense and stable emission but also resistance to interference from complex biological environments (*e.g.*, diverse ions) and appropriate biocompatibility.[3,4] Additionally, theranostic MOFs, which integrate diagnostic imaging and therapeutic effects, have garnered increasing attention, as they can achieve real-time monitoring of treatment responses while delivering therapeutic efficacy. However, balancing luminescent brightness, environmental stability, biocompatibility, and cell-type

[a]*College of Public Health, Key Laboratory of Environmental Factors and Chronic Disease Control, Ningxia Medical University, Yinchuan 750004, China. E-mail: 13895400691@163.com*

[b]*State Key Laboratory of High-Efficiency Utilization of Coal and Green Chemical Engineering, College of Chemistry and Chemical Engineering, Ningxia University, Yinchuan 750021, China*

† These authors contributed equally to this work.

adaptability in a single MOF system remains a key challenge. Moreover, the structure–property relationships underlying the photophysical and biological behaviors of Zn(II)-MOFs, such as how coordination geometry and framework architecture influence fluorescence quantum yield, subcellular localization, and cytotoxicity, are not fully elucidated, limiting the rational design of functional MOF-based bioprobes.[5–7]

To address these challenges, Zn(II) is selected as the metal center to coordinate to 2,5-dihydroxyterephthalic acid (DHTA) and 1,4-bis[(1*H*-imidazol-1-yl)methyl]benzene (bix) mixed ligands. DHTA possesses both carboxyl and hydroxyl functional groups: the oxygen atoms from the carboxyl groups exhibit diverse coordination modes, which facilitate the formation of stable coordination bonds between transition metal ions and organic linkers. Moreover, the strong binding ability of the carboxyl groups (derived from carboxylate ligands) can effectively inhibit the coordination of metal centers with water molecules, thereby preventing the luminescence quenching of MOFs. Additionally, oxygen-containing functional groups generally enhance the hydrophilicity of MOFs, which is conducive to achieving low toxicity and good biocompatibility.[8,9] In contrast, imidazole-based ligands (*e.g.*, bix) can significantly improve the thermal and chemical stability of MOFs through their strong coordination ability, rigid conjugated frameworks, and tunable spatial/electronic effects. Specifically, the two nitrogen atoms on the imidazole ring possess lone electron pairs, serving as strong electron-donating sites to form stable coordination bonds with metal ions; the planar structure of the imidazole ring also promotes intermolecular π–π stacking interactions. Furthermore, the conjugated structure of the imidazole ring constructs a stable, rigid framework, which reduces intramolecular vibrations and rotations, decreases the probability of non-radiative transitions, and ultimately enhances the efficiency and intensity of fluorescence emission.[10,11]

Here, we synthesize two Zn(II)-based MOFs (**1** and **2**) with different structures modulated by reactant loads and autoclave filling degrees. The crystal structures, thermal stability, luminescent performance, and ionic interference resistance of both compounds are systematically characterized. The biological functionalities of both compounds, including cytotoxicity, subcellular localization, and imaging capability, are evaluated in three cancer cell lines (HeLa, SH-SY5Y, and A549). Furthermore, we explore the structure–property relationships to reveal how the more ideal tetrahedral coordination geometry and interpenetrated 3D framework of compound **2** contribute to the superior fluorescence properties and versatile biological performance. This work provides valuable insights for the rational design of MOF-based materials with tailored functionalities for bioimaging and theranostic applications.

Materials and methods

Reagents and instruments

All reagents and solvents were of analytical grade and used as received from commercial suppliers. HeLa, SH-SY5Y, and A549 cells were procured from Shanghai Zhong Qiao Xin Zhou Biotechnology Co., Ltd (China). Fourier-transform infrared (FT-IR) spectra (4000–400 cm^{-1}) were recorded on a Shimadzu spectrometer using the KBr pellet method. Elemental analyses (C, H, N) were performed on a PerkinElmer 2400 CHN analyzer. Powder X-ray diffraction (PXRD) patterns were collected on a Rigaku RU-200 diffractometer (Cu Kα radiation, $\lambda = 1.5406$ Å) operating at 60 kV and 300 mA, with a scanning rate of 5° min^{-1} and a step size of 0.02° in 2θ. Thermogravimetric analysis (TGA) was conducted on a NETZSCH STA 449F3 instrument under a nitrogen atmosphere, heating samples from 30 °C to 700 °C at a rate of 10 °C min^{-1}, with an empty Al_2O_3 crucible as reference. Steady-state fluorescence spectra were acquired at room temperature using an Edinburgh F-7000 spectrofluorometer. Cellular imaging and fluorescence colocalization studies were carried out on a Zeiss LSM 900 laser scanning confocal microscope.

Synthesis of $[Zn(DHTA)_2(bix)_2]$ (1)

A mixture of $Zn(NO_3)_2 \cdot 6H_2O$ (0.0298 g, 0.1 mmol), H_2DHTA (0.0396 g, 0.2 mmol), and bix (0.0476 g, 0.2 mmol) was dissolved in a solvent mixture of anhydrous ethanol (2 mL) and deionized water (8 mL). The solution was transferred to a 15 mL Teflon-lined stainless-steel autoclave and heated at 140 °C for 72 h, followed by slow cooling to room temperature. Yellow block crystals of **1** were collected by filtration, washed with ethanol, and dried in air. Yield: 58% (based on Zn). Anal. calcd for $C_{22}H_{18}N_4O_6Zn$: C, 52.87; H, 3.63; N, 11.21. Found: C, 52.85; H, 3.60; N, 11.23. Selected IR data (KBr, cm^{-1}): 3132 (m), 1609 (s), 1522 (m), 1489 (m), 1420 (m), 1381 (m), 1242 (s), 1094 (s), 1032 (m), 953 (s), 866 (m), 816 (m), 787 (m), 737 (m), 656 (s), 590 (m), and 419 (m).

Synthesis of $[Zn(DHTA)_2(bix)_2]$ (2)

Compound **2** was synthesized following the same procedure as for **1**, but with scaled-up quantities: $Zn(NO_3)_2 \cdot 6H_2O$ (0.1192 g, 0.4 mmol), H_2DHTA (0.1584 g, 0.8 mmol), bix (0.1904 g, 0.8 mmol), anhydrous ethanol (8 mL), and deionized water (32 mL) were placed in a 50 mL autoclave. After the same thermal treatment, yellow prismatic crystals of **2** were obtained. Yield: 75% (based on Zn). Anal. calcd for $C_{22}H_{18}N_4O_6Zn$: C, 52.87; H, 3.63; N, 11.21. Found: C, 52.86; H, 3.64; N, 11.20. Selected IR data (KBr, cm^{-1}): 3136 (m), 1609 (s), 1522 (m), 1489 (m), 1420 (m), 1381 (m), 1242 (s), 1094 (s), 1032 (m), 953 (s), 866 (m), 816 (m), 787 (m), 737 (m), 656 (s), 590 (m), and 419 (m).

Single crystal X-ray diffraction measurements

A suitable single crystal was selected and mounted for X-ray diffraction analysis. Diffraction data were collected at room temperature on a Bruker SMART APEX-CCD diffractometer equipped with graphite-monochromated Mo Kα radiation ($\lambda =$ 0.71073 Å). Additional data sets were collected in the temperature range of 140–320 K using Cu Kα radiation ($\lambda = 1.54178$ Å). The structure was solved using intrinsic phasing methods with SHELXT and refined by full-matrix least-squares on F^2 with SHELXL.[12] All calculations were performed through the OLEX2 interface.[13] Non-hydrogen atoms were refined anisotropically,

and hydrogen atoms were placed at calculated positions and refined using a riding model. The crystal parameters and details of the structure refinement are summarized in Table S1. The Cambridge Crystallographic Data Centre (CCDC) deposition numbers for compounds **1** and **2** are 2455666 and 2455667, respectively.

Fluorescence stability against ionic interference

To evaluate the fluorescence stability, the sensing experiments were conducted against a series of common cations and anions. The tested cations included Ca^{2+}, Cd^{2+}, Co^{2+}, Cr^{3+}, Cu^{2+}, Fe^{3+}, Li^{+}, Na^{+}, Ni^{2+}, Pb^{2+}, and K^{+} [as $M(NO_3)_x$, $C = 0.01$ mol L^{-1}]. The tested anions included Br^{-}, $Cr_2O_7^{2-}$, CrO_4^{2-}, HPO_4^{2-}, NO_3^{-}, PO_4^{3-}, $S_2O_8^{2-}$, and SO_4^{2-} [as potassium or sodium salts, $C = 0.01$ mol L^{-1}]. For the experiments, aqueous suspensions of compounds **1** and **2** were first prepared by ultrasonically dispersing finely ground powder (5 mg) in deionized water (5 mL) for 30 minutes. Subsequently, fluorescence titration was performed by gradually adding incremental aliquots of the prepared cationic or anionic aqueous solutions into the well-dispersed suspensions of **1** or **2**, and the corresponding fluorescence spectra were recorded after each addition. During all fluorescence assays, phosphate-buffered saline (PBS) was used to maintain the pH at 7.0.

Cell culture and cell viability assay

The human cancer cell lines HeLa, SH-SY5Y, and A549 were cultured in Dulbecco's Modified Eagle Medium (DMEM) supplemented with 10% fetal bovine serum (FBS) and 1% penicillin-streptomycin. Cells were maintained at 37 °C in a humidified atmosphere containing 5% CO_2. For the cytotoxicity assay, cells were seeded in 96-well plates at a density of 5×10^4 cells per well and allowed to adhere for 24 hours. Subsequently, the cells were treated with fresh medium containing different concentrations (0, 10, 20, 50, and 100 μmol L^{-1}) of compounds **1** or **2** for 24 hours. Each concentration, including the solvent control (0 μmol L^{-1}), was tested in five replicate wells, and the entire experiment was performed in duplicate. After the treatment period, the compound-containing medium was removed. Cell viability was then assessed using the Cell Counting Kit-8 (CCK-8) assay. Briefly, 10 μL of CCK-8 reagent and 100 μL of fresh DMEM were added to each well, followed by incubation at 37 °C for 1 hour.[14] The absorbance of each well at 450 nm was measured using a Thermo Scientific microplate reader. Cell viability was calculated as a percentage relative to the untreated control group using the formula: Viability (%) = [(OD treated − OD blank)/(OD control − OD blank)] × 100. Data are presented as the mean ± standard deviation (SD).[15]

Confocal microscopic imaging of incubated cells

On the day prior to imaging, cells were seeded onto coverslips placed in a 24-well plate at a density of 1×10^5 cells per well. On the day of treatment, the cells were incubated with compound **1** or **2** at a final concentration of 10 μmol L^{-1} for 4 hours at 37 °C. Subsequently, the cells were washed three times with phosphate-buffered saline (PBS) to remove any unabsorbed complexes and then fixed with 4% paraformaldehyde at 37 °C for 20 minutes. After removing the fixative, the cells were gently rinsed three times with PBS. Next, the nuclei were stained by incubating the cells with Hoechst 33258 dye (5 μg mL^{-1}, 500 μL per well) for 15 minutes in the dark. After staining, the dye solution was discarded, and the cells were washed three more times with PBS.[16] The coverslips were then carefully removed using fine-tip tweezers, inverted, and mounted onto clean glass slides using an antifade mounting medium to minimize fluorescence quenching and bubble formation. Cell images were acquired using a laser scanning confocal microscope. The Hoechst 33258 channel and the corresponding channels for the compounds were excited with a 405 nm laser to visualize nuclear staining and compound localization, respectively.

Computational details

The ground-state geometries of the molecular building blocks (asymmetric units) extracted from the single-crystal structures of compounds **1** and **2**, as well as the free ligands, were optimized using density functional theory (DFT) at the B3LYP/6-31G(d,p) level. All calculations were performed with the Gaussian 09 program package. The highest occupied molecular orbital (HOMO) and the lowest unoccupied molecular orbital (LUMO) energies were obtained from the optimized structures to evaluate their energy gaps.

Results and discussion

Structural description of compounds 1 and 2

The schematic for the construction of compounds **1** and **2** is shown in Scheme 1. Single-crystal X-ray diffraction (SC-XRD) was employed to determine the crystal structures of compounds **1** ($C_{22}H_{18}N_4O_6Zn$) and **2** ($C_{22}H_{18}N_4O_6Zn$) (Table S1). Featuring Zn(II) as the central metal ion, compounds **1** and **2** crystallized in different crystal systems and space groups. Compound **1** crystallized in the triclinic crystal system with the $P\bar{1}$ space group, whereas compound **2** belonged to the monoclinic crystal system with the $C2/c$ space group. The asymmetric units of both compounds **1** and **2** consisted of one crystallographically independent Zn(II) ion, two 2,5-deprotonated H_2DHTA^{2-} ligands, and two bix ligands. Each Zn(II) center was four-coordinate, with a coordination sphere composed of two carboxylate O atoms from DHTA and two N atoms from bix (N_2O_2 donor set), resulting in a tetrahedral coordination

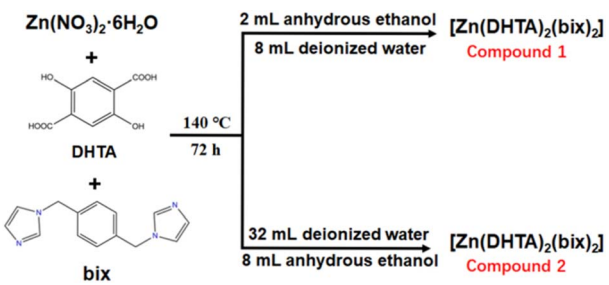

Scheme 1 Schematic of the synthesis of compounds **1** and **2**.

geometry. The Continuous Shape Measure (CShM) values were 1.097 (**1**) and 0.398 (**2**), respectively. Compound **2** exhibited a coordination structure much closer to the ideal tetrahedron than compound **1**. Bond lengths and bond angles for both compounds are summarized in Tables S2 and S3. Compounds **1** and **2** exhibited average Zn–N bond lengths of 2.000 Å and 1.995 Å, as well as average Zn–O bond lengths of 1.957 Å and 1.951 Å, respectively. The most notable structural difference between the two compounds lies in their extended frameworks. The constitutional units of compound **1** were further bridged by carboxylate O atoms of DHTA ligands *via* a monodentate coordination mode, forming a two-dimensional (2D) grid-like layered structure. Furthermore, π–π stacking interactions between adjacent 2D layers were assembled into a three-dimensional (3D) supramolecular architecture (Fig. S1). For compound **2**, the coordination units propagated into 1D "Z"-shaped chains. Then, bix ligands bridged the chains *via* monodentate N coordination, yielding a 2D grid layer. Interpenetration between the layers afforded a 3D supramolecular architecture (Fig. 1). Notably, in compound **1**, the imidazolyl rings of adjacent bix ligands underwent offset face-to-face π–π stacking interactions, with a centroid-to-centroid distance of 3.71 Å (Fig. S1e).[17,18] In theory, such interactions not only enhance the stability of the supramolecular layered structure but also potentially contribute to the fluorescence performance discrepancy between compounds **1** and **2**.

Subtle discrepancies in synthesis protocols accounted for the structural distinctions observed between compounds **1** and **2**. For compound **1**, relatively low reactant loads were used: 0.1 mmol $Zn(NO_3)_2 \cdot 6H_2O$ and 0.2 mmol each of DHTA and bix ligands. The reaction was carried out in a 15 mL autoclave with 10 mL of solvent, corresponding to a filling degree of 66.7%. In this low-volume system, the high heat transfer efficiency of the solution enhanced the nucleation rate. Additionally, the constrained growth space facilitated the formation of dense two-dimensional (2D) structures with strong π–π stacking interactions.[19,20] Conversely, compound **2** was synthesized with a four-fold increase in reactant amounts: 0.4 mmol $Zn(NO_3)_2 \cdot 6H_2O$, 0.8 mmol DHTA, and 0.8 mmol bix. The reaction was conducted in a 50 mL autoclave with 40 mL of solvent, resulting in an elevated filling ratio of 80%. In this high-volume system, diminished thermal convection and mass transfer efficiency decelerated crystal growth kinetics. The slowed growth provided layered structures, with ample time to optimize their arrangement, eventually yielding an interpenetrated 3D framework.[21,22]

FT-IR, PXRD, stability analysis

Fourier transform infrared (FTIR) spectra of DHTA, bix ligands, and both compounds are displayed in Fig. S2. For the DHTA ligand, the broad band in the range of 3300–2500 cm^{-1} and the intense peak around 1700 cm^{-1} were assigned to the O–H and C=O stretching vibrations of the carboxylic acid group,

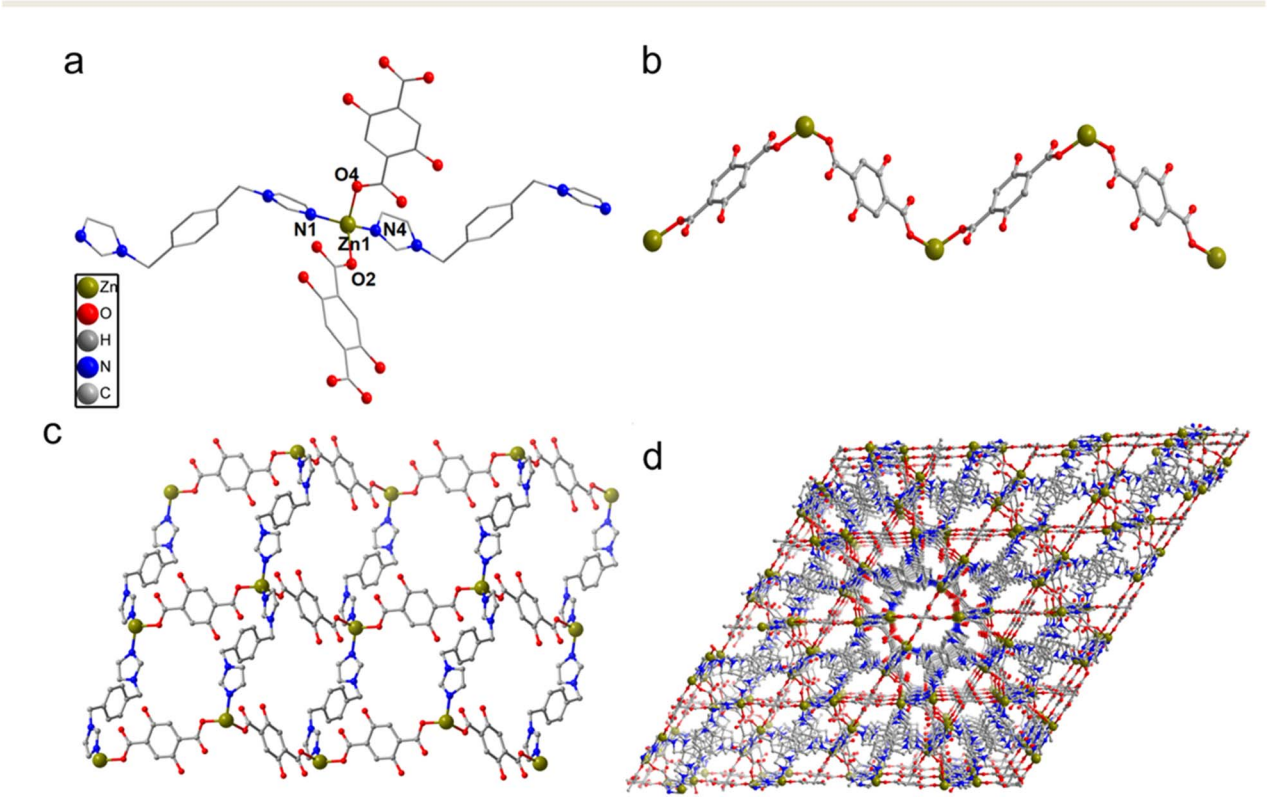

Fig. 1 (a) Coordination environment and geometric configuration of Zn(II) in **2**. (b) 1D chains of **2**. (c) 2D layer of **2**. (d) Supramolecular 3D structure of **2**. All hydrogen atoms for **2** are omitted for clarity.

respectively. After coordination, a significant narrowing of this broad band was observed in compounds **1** and **2**, indicative of carboxyl group deprotonation. The characteristic symmetric (COO^-) and antisymmetric (COO^-) stretching vibrations of the carboxylate group were detected at 1340–1490 cm^{-1} and 1520–1650 cm^{-1}, respectively, confirming carboxylate oxygen coordination to Zn(II) ions. For the bix ligand, a broad peak near 3250 cm^{-1} was assigned to N–H stretching, and peaks in the 1500–1600 cm^{-1} region resulted from C=N stretching vibrations. The presence of C=N absorption peaks at 450–550 cm^{-1} in compounds **1** and **2** implied the participation of imidazole nitrogen atoms in coordination with Zn(II).

Powder X-ray diffraction (PXRD) was employed to verify the phase purity of as-synthesized compounds **1** and **2**. Fig. S3 shows that the experimental PXRD patterns of compounds **1** and **2** closely match the simulated patterns from single-crystal data, verifying the phase purity of the bulk materials. Small variations in peak intensity resulted from the preferred orientation of microcrystals.

Thermogravimetric analysis (TGA) was conducted under a nitrogen atmosphere over the temperature range of 30–800 °C to assess the thermal stability of the compounds (Fig. S4). Compounds **1** and **2** underwent analogous two-step decomposition: a rapid, significant weight loss commencing at approximately 330 °C, followed by a slow, sustained weight loss. The first decomposition step mainly resulted from the breakdown of the organic ligands. The high thermal stability of both compounds stemmed from the rigid, conjugated backbone of the bix ligand and the strong coordination bonds formed between electronegative carboxylate oxygen atoms and Zn(II) ions. Significantly, beyond approximately 420 °C, compound **2** underwent a slower weight loss than compound **1**, demonstrating superior thermal stability. The improvement was ascribed to the resilient 3D interpenetrated framework of **2**, which was constructed from interconnected layers. In contrast, the 3D supramolecular structure of compound **1** was primarily stabilized by relatively weak π–π stacking interactions between its 2D layers, resulting in relatively fast decomposition at elevated temperatures.[23] To investigate the aqueous stability of compounds **1** and **2**, the samples were soaked in aqueous solutions with pH = 3–11. PXRD results showed that the position and intensity of the characteristic diffraction peaks of the treated samples exhibited no obvious changes and were highly consistent with those of the as-synthesized samples and the simulated patterns from single-crystal data (Fig. S5). This indicated that the crystalline frameworks of the materials did not collapse or undergo structural transformation within the tested pH range, revealing excellent acid–base stability.

Luminescence properties

Under 365 nm ultraviolet (UV) irradiation, both compounds **1** and **2** emitted intense green fluorescence that was visible to the naked eye (Fig. S7). The solid-state excitation and emission spectra of the compounds were contrasted with those of free DHTA and bix ligands (Fig. S6). The ligand-centered fluorescence of DHTA ($\lambda = 480$ nm, $\lambda = 425$ nm) and bix ($\lambda = 508$ nm, $\lambda = 440$ nm) stemmed from intraligand π*–n or π–π* transitions. Upon coordination to Zn(II), significant red shifts in fluorescence emission were detected. Compound **1** exhibited a broad emission maximum at 530 nm ($\lambda = 394$ nm), corresponding to red shifts of 50 nm relative to DHTA and 22 nm relative to bix. Compound **2** displayed a further red-shifted emission maximum at 540 nm ($\lambda = 402$ nm), with respective red shifts of 60 nm (*vs.* DHTA) and 32 nm (*vs.* bix). Owing to the redox-inert characteristic of d^{10} Zn(II) ions, the red shifts resulted from the generation of intraligand or interligand charge-transfer (CT) excited states. Ligand coordination induced the effective reorganization of DHTA and bix electron clouds, leading to narrow energy gaps in both compounds (Fig. S12), which fundamentally tuned the emission colors. The photophysical parameters further highlighted the superiority of compound **2**. Photophysical data underscored the advantage of compound **2**. Compound **2** possessed a markedly higher fluorescence quantum yield ($\Phi = 13.78\%$) compared to compound **1** ($\Phi = 6.02\%$).[24] The fluorescence lifetime decay curves of compounds **1** and **2** were fitted with a bi-exponential function, and the goodness-of-fit parameter (R^2) was close to 1, indicating an excellent fitting quality. It was obtained by the average lifetime formula: $((\tau_{avg}) = (A_1\tau_1^2 + A_2\tau_2^2)/(A_1\tau_1 + A_2\tau_2))$ that the average lifetime of **1** was 0.83 μs, and the average lifetime of **2** was 0.98 μs (Fig. S8).

The fluorescence spectra of both compounds were also measured in aqueous solution at 298 K (25 °C). Compound **1** maintained an emission maximum at approximately 530 nm, whereas compound **2** showed an 18 nm blue shift in water compared to the solid-state emission profile (Fig. S7). This implies that the highly symmetric tetrahedral configuration in the crystal of **2** may experience local structural distortion in solution, potentially driven by coordination or hydrogen-bonding interactions with water. Such solvent-induced structural distortion may modulate the energy of metal–ligand or ligand-centered transitions, resulting in the observed spectral shift.

To summarize, both Zn(II) complexes exhibit strong green emission, which renders them applicable for fluorescence imaging purposes. Compound **2** distinguished itself with a relatively high fluorescence quantum yield and more red-shifted emission, advantages structurally attributed to a more ideal tetrahedral coordination geometry. Additionally, the stable fluorescence of **2** in aqueous media reinforced its viability as a potential candidate for cellular imaging.

Fluorescence stability against ionic interference

In the context of applying Zn(II)-based compounds for cancer cell imaging, maintaining fluorescence stability in complex ionic milieus is essential, given that various biological ions may trigger fluorescence quenching. To assess this fluorescence stability, we examined the fluorescence responses of both compounds to a panel of common biological cations and anions. Cations tested were Ca^{2+}, Cd^{2+}, Co^{2+}, Cr^{3+}, Cu^{2+}, Fe^{3+}, Li^+, Na^+, Ni^{2+}, Pb^{2+}, and K^+, supplied as nitrate derivatives $[M(NO_3)_x]$, with a final concentration of 0.01 mol L^{-1}. Anions

examined were Br^-, $Cr_2O_7^{2-}$, CrO_4^{2-}, HPO_4^{2-}, NO_3^-, PO_4^{3-}, $S_2O_8^{2-}$, and SO_4^{2-}, prepared as potassium or sodium salts, with a concentration of 0.01 mol L^{-1}. Fluorescence recognition experiments showed that both compounds did not experience notable fluorescence quenching when exposed to any of the aforementioned ions (Fig. S9 and S10). Furthermore, compound **2** consistently displayed higher fluorescence emission intensity than compound **1** across all tested ionic conditions. Taken together, these findings illustrated that the compounds possessed outstanding interference resistance and stable fluorescence traits in the presence of diverse potential ionic quenchers. Such robust fluorescence stability in ionic environments lays a solid experimental groundwork for their trustworthy use in subsequent cancer cell imaging, wherein intracellular ion levels and species fluctuate considerably.[25,26]

Cytotoxicity evaluation and cell death mechanism investigation

Owing to the luminescent characteristics and good aqueous stability of both compounds, the applicability of **1** and **2** as cell imaging agents was assessed in three cancer cell lines: HeLa (Henrietta Lacks cervical adenocarcinoma), SH-SY5Y (human bone marrow neuroblastoma), and A549 (human lung carcinoma). The cytotoxic effects of the compounds were first evaluated *via* the Cell Counting Kit-8 (CCK-8) assay following 24 h of incubation. Cell viability was measured over a concentration range of 10–150 μmol L^{-1}; the inhibitory effect on cell proliferation was quantified, and the half-maximal inhibitory concentration (IC_{50}) was calculated for each compound. The IC_{50} value, defined as the compound concentration required to reduce cell viability by 50%, serves as a critical indicator of cytotoxicity, with a low IC_{50} value indicating high cytotoxic potency.[27,28] One-way analysis of variance (ANOVA) was used for statistical analysis, with pairwise comparisons between each experimental group and the control group (Fig. 2). *In vitro* cytotoxicity assays uncovered distinct activity profiles for the two compounds. Against HeLa cells (Fig. 2a), compound **1** displayed strong cytotoxicity, with viability dropping to 48.1% at 10 μmol L^{-1} and further decreasing to 25.1% at 150 μmol L^{-1}, corresponding to an IC_{50} of 19.71 ± 3.65 μmol L^{-1}. Conversely, compound **2** displayed negligible toxicity, with viability remaining above 80% across the entire concentration range up to 150 μmol L^{-1} (IC_{50} > 150 μmol L^{-1}), underscoring the suitability as a biocompatible imaging agent. Against SH-SY5Y cells, both compounds suppressed proliferation but with distinct potencies, exhibiting IC_{50} values of 53.37 ± 4.95 μmol L^{-1} for **1** and 42.40 ± 7.05 μmol L^{-1} for **2** (Fig. 2b). At 10 μmol L^{-1}, cell viability remained at 80% for compound **1** and 70% for compound **2**, indicating acceptable biocompatibility at this concentration. Cell viability declined sharply between 50 and 100 μmol L^{-1}, reaching 15.8% for compound **1** and 28.7% for compound **2** at the maximum concentration of 150 μmol L^{-1}. Against A549 cells, compound **2** caused a rapid reduction in viability to 56.6% at 10 μmol L^{-1}, with a subsequent gradual decrease to 44.9% at 150 μmol L^{-1} (Fig. 2c). Despite an IC_{50} value > 150 μmol L^{-1}, this significant viability reduction at low concentrations suggested a distinct mode of action and implied potential therapeutic utility against A549 cells. Significant inhibitory effects ($P < 0.05$) were confirmed across various concentrations for both compounds in HeLa/SH-SY5Y cells and for compound **2** in A549 cells. Critically, acute cell death was undetectable in most cells after a 24 h treatment period, including at the maximum concentration of 150 μmol L^{-1}. Such acceptable biocompatibility at low concentrations provided a robust basis for the subsequent cell imaging studies.

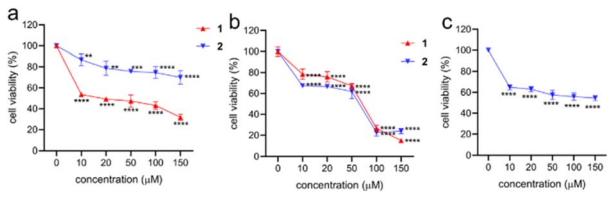

Fig. 2 (a) Proliferation rate of HeLa cells treated with different concentrations of **1** and **2**. (b) Proliferation rate of SH-SY5Y cells treated with different concentrations of **1** and **2**. (c) Proliferation rate of A549 cells treated with different concentrations of **2**. *$P < 0.05$.

Given the notably low IC_{50} value of **1** against HeLa cells, we further explored the cytotoxic mechanism of **1** by analyzing cellular ultrastructural morphology *via* transmission electron microscopy (TEM). As presented in Fig. S11, treated HeLa cells display characteristic signs of apoptosis (*e.g.*, nuclear shrinkage, irregularity, chromatin condensation, and apoptotic bodies) and ferroptosis (*e.g.*, mitochondrial shrinkage, reduced/absent cristae, and enhanced membrane density). The concurrent indicators of endoplasmic reticulum (ER) stress (dilated rough endoplasmic reticulum (RER) with ribosome degranulation) and autophagy activation (abundant autophagic vacuoles) are also detected.[29] Collectively, these ultrastructural alterations demonstrate the co-activation of multiple cell death pathways,[30] wherein ferroptosis-associated lipid peroxidation may exacerbate ER stress, thereby facilitating apoptotic cell death.[31,32]

Cellular imaging and localization studies

The aforementioned cytotoxicity results demonstrated that compound **2** maintained high cell viability (>70%) across all tested cell lines at concentrations ≤ 10 μmol L^{-1}, establishing a necessary biocompatibility window for the application as a bioimaging probe. Thus, 10 μM (equivalent to 10 μmol L^{-1}) was selected as the representative working concentration for subsequent cellular imaging experiments, with the goal of evaluating the subcellular localization while avoiding significant acute cytotoxicity. Following this, *in vitro* imaging experiments were carried out on HeLa, SH-SY5Y, and A549 cells to align with the earlier cytotoxicity evaluation system. After co-incubation with compound **1** or **2** (10 μM) for 4 hours, cells were stained with Hoechst 33258 (a nuclear marker) to determine the intracellular localization of the compounds. Confocal laser scanning microscopy (CLSM) images were acquired under 405 nm laser excitation (Fig. 3 and 4).

As illustrated in Fig. 3, the fluorescence signal of compound **1** was uniformly distributed across the cytoplasm and nucleus

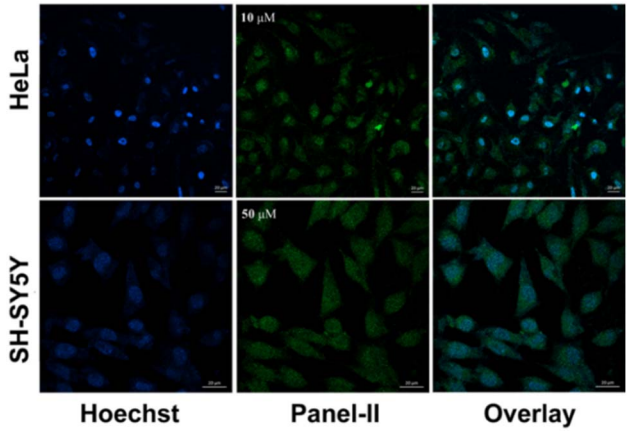

Fig. 3 Confocal laser scanning microscopy images of two cancer cells treated with **1** and Hoechst 33258 dye (5 μg mL^{-1}). Note: (left) nuclear staining image; (middle) cell staining image after reacting with **1**; and (right) merged image; scale bar = 20 μm.

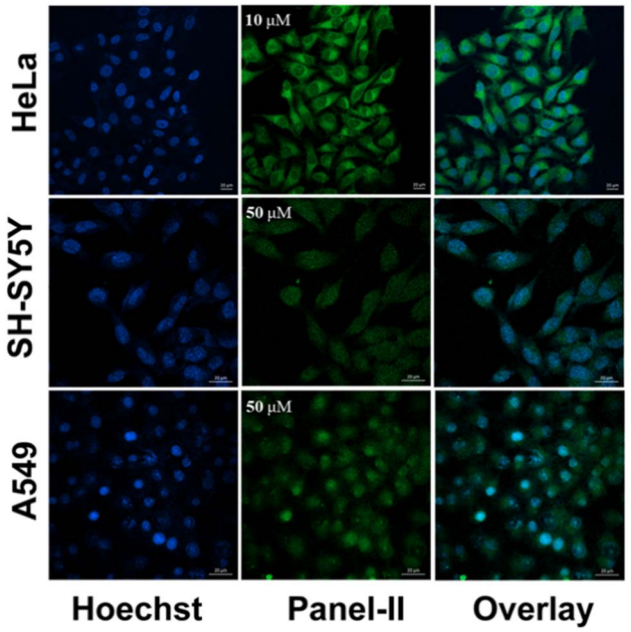

Fig. 4 Confocal laser scanning microscopy images of three cancer cells treated with **2** and Hoechst 33258 dye (5 μg mL^{-1}). Note: (left) nuclear staining image; (middle) cell staining image after reacting with **2**; and (right) merged image; scale bar = 20 μm.

in both HeLa and SH-SY5Y cell lines, which was consistent with prior imaging experimental settings. The nuclear signal of compound **1** fully overlapped with Hoechst 33258 (exhibiting cyan in the merged image), confirming its robust nuclear targeting capacity. This distribution pattern suggests that the densely packed two-dimensional layered structure of compound **1** may facilitate passive diffusion across the nuclear membrane, while π–π stacking interactions likely enhance the structural stability and alleviate aggregation-caused quenching (ACQ).[33,34] Compound **2** exhibited cell-type-dependent subcellular localization (Fig. 4), differing from the consistent cytoplasm-nucleus distribution of compound **1**. In HeLa cells, compound **2** showed a predominantly cytoplasmic fluorescence distribution, with intense perinuclear signals and negligible overlap with Hoechst 33258-stained nuclei (blue in the merged image). In contrast, in both SH-SY5Y and A549 cells, the fluorescence of compound **2** was uniformly distributed across the cytoplasm and nucleus, exhibiting significant colocalization with Hoechst 33258 in the nuclei (appearing bright cyan in the merged images). Collectively, compound **2** exhibited the capacity to image a broad spectrum of cell types, which was attributed to its adaptive localization profile.

Combined with its superior intrinsic fluorescence intensity and quantum yield confirmed previously, it delivered clearer, more robust imaging signals relative to compound **1**.[35,36]

Notably, in the SH-SY5Y cells, both compounds display uniform signal distribution across cellular compartments, which may correlate with the high membrane fluidity characteristic of specific cancer cell lines. Integrating the cytotoxicity and imaging (Fig. 2–4) data, both compounds exhibited a unique "concentration-dependent dual functionality" in the SH-SY5Y cells. At ≤10 μmol L^{-1}, both compounds retained high cell viability and demonstrated robust fluorescence imaging capability, while at ≥50 μmol L^{-1}, they exhibited marked inhibition of cell proliferation.[37] The results highlighted that, especially in the SH-SY5Y cells, both compounds could be developed into theranostic agents with concentration-tunable diagnostic imaging and therapeutic functionalities, serving as integrated diagnosis-therapy platforms.

MOFs can enter cells through a range of mechanisms, with endocytosis being the most commonly reported pathway. This process is influenced by the key physicochemical properties of the MOFs, such as particle size and functional groups. Positively charged, nanoscale MOFs often show enhanced interaction with the negatively charged cellular membrane, facilitating internalization through endocytic or micropinocytic routes. Once internalized, MOFs are typically trafficked to the cytoplasm or nucleus compartments, depending on the uptake pathway.[38] Therefore, the appropriate particle sizes of the **1** and **2** were calculated from the PXRD patterns using Debye–Scherrer equation:[39] $\tau = K\lambda/\beta \cos\theta$, where τ is the crystal size of material perpendicular to the lattice planes, K is a numerical factor frequently referred to as the crystallite shape factor, λ is the wavelength of the X-ray, β is the width (full-width at half maximum) of the X-ray diffraction peak in the radians, and θ is the Bragg angle. For the calculation, the strongest peak of each compound was selected, and the full width at half maximum (FWHM) of the peaks was determined from the PXRD data. The FWHM values for **1** and **2** were 0.22 and 0.14, respectively, corresponding to the peaks at 19.36° and 9.6°. The particle size of **1** is 36 nm and that of **2** is 56 nm. For effective use in cell imaging, the material must exhibit a nanoscale particle size and good solubility in water. According to the Debye–Scherrer formula, the size of both MOFs is <100 nm. However, **1** formed a suspension in water, whereas **2** showed good solubility in water, indicating that **2** is a more ideal compound for cellular imaging.[40]

Discussion on structure–property relationships

The comprehensive dataset demonstrated that the superior photophysical performance of compound **2** stemmed from its more optimal tetrahedral coordination geometry. Electronically, this structural merit translated to a reduced HOMO–LUMO gap (3.86 eV *vs.* 3.96 eV for compound **1**; Fig. 5), which was directly associated with its red-shifted emission (540 nm *vs.* 530 nm) and approximately two-fold higher fluorescence quantum yield (13.78% *vs.* 6.02%).[41–43] In luminescent materials, such as Zn-MOFs, the origin of fluorescence emission lies in the transition of electrons from the LUMO (lowest unoccupied molecular orbital) back to the HOMO (highest occupied molecular orbital), accompanied by the release of photons. According to the formula: $E = hc/\lambda$, photon energy is inversely proportional to wavelength. A small bandgap corresponds to a small energy-level difference between the HOMO and LUMO; thus, the energy released by electron transition is relatively low, resulting in a high emission wavelength (*i.e.*, red shift). In this study, the coordination of Zn(II) ions with ligands promoted the effective rearrangement of the ligand electron clouds, rather than the fluorescence enhancement being attributed solely to the "reduction in bandgap". It was the combined effect of optimized coordination structure and reduced bandgap that led to a simultaneous improvement in fluorescence intensity and quantum yield.[44–46]

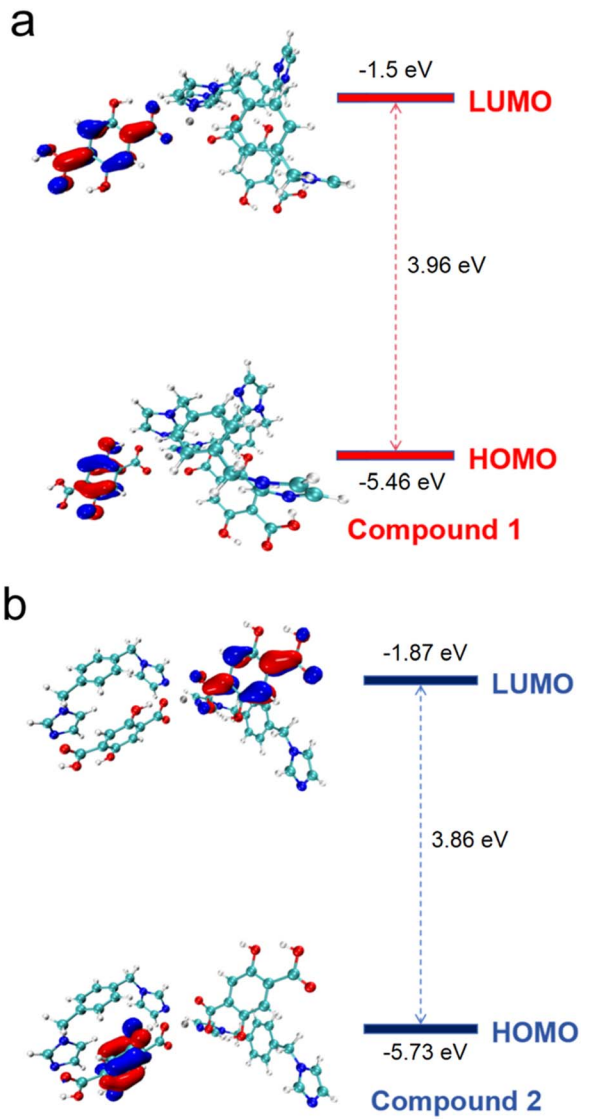

Fig. 5 Energy-level diagram of compounds **1** (a) and **2** (b).

Notably, the intrinsic improvement conferred robust functional advantages across diverse application scenarios. First, in fluorescence sensing assays with a broad panel of cations and anions, compound **2** consistently displayed higher emission intensity than compound **1**, indicating that the symmetric structure of **2** not only enhanced intrinsic luminescence but also imparted greater stability against potential quenching interferents. Most importantly, these superior photophysical properties directly underpinned the excellent performance of **2** in biological imaging applications, consistent with prior confocal imaging results. The enhanced brightness and stability of compound **2** emission offered a tangible, practical benefit for confocal microscopy applications. Compound **2** effectively imaged all three tested cancer cell lines (HeLa, SH-SY5Y, and A549) with distinct, stable signals, showcasing expanded applicability.

Additionally, the cell-type-specific localization profiles (*e.g.*, cytoplasmic in HeLa *vs.* nuclear colocalization in SH-SY5Y/A549) of **2** and the confirmed concentration-dependent theranostic window in the SH-SY5Y cells highlighted the functional complexity for **2**, derived from a flexible yet stable molecular architecture. Thus, the optimized structure of **2** was the cornerstone of the comprehensive superiority, encompassing fundamental electronic properties, stability in complex milieus, and effective, dependable performance as a versatile luminescent material for sensing and bioimaging.[47–49]

Conclusions

In summary, two Zn(II)-based MOFs (compounds **1** and **2**) were synthesized *via* tailored hydrothermal methods, with structural differences rooted in reactant loads and autoclave filling degrees. Compound **1** formed a 3D supramolecular architecture stabilized by π–π stacking between 2D layers, while compound **2** assembled into an interpenetrated 3D framework with a more ideal tetrahedral Zn(II) coordination geometry. Both compounds exhibited green fluorescence with ligand-centered charge-transfer origins and maintained robust fluorescence stability against diverse biological ions, with compound **2** showing superior emission intensity across all ionic conditions. Biologically, compound **1** exhibited potent cytotoxicity against the HeLa cells, whereas compound **2** was highly biocompatible in the HeLa cells, making it an ideal imaging agent. In the SH-SY5Y cells, both compounds showed concentration-dependent dual functionality—low concentrations enabled imaging, while high concentrations inhibited proliferation. Compound **2** further exhibited cell-type-adaptive subcellular localization, enabling the clear imaging of the HeLa, SH-SY5Y, and A549 cells. This work not only highlights that subtle synthetic

modifications tune framework architecture and coordination geometry to optimize photophysical and biological performances, but also provides valuable insights for the rational design of MOF-based materials with tailored functionalities for sensing, bioimaging, and cancer therapy.

Conflicts of interest

There are no conflicts to declare.

Data availability

CCDC 2455666 (**1**) and 2455667 (**2**) contain the supplementary crystallographic data for this paper.[50a,b]

All data supporting this article have been included in the manuscript or included as part of the supplementary information (SI). Supplementary information: additional experimental data, crystallographic data, additional figures and tables, and optical data. See DOI: https://doi.org/10.1039/d6ra02099b.

Acknowledgements

This work was supported by the National Natural Science Foundation of China (22063008 and 22463010), the Full-time Recruitment Program for High-level Talents (2024BEH04153), the Youth Talents Supporting Program of Ningxia Province, and the Graduate Innovative Experiment and the Discipline Project of the Ningxia Medical University (X2025107520014).

References

1 J. Pantwalawalkar, P. Mhettar, S. Nangare, R. Mali, A. Ghule, P. Patil, S. Mohite, H. More and N. Jadhav, *ACS Biomater. Sci. Eng.*, 2023, **9**, 4497–4526.
2 Y. Zhao, X. Jiang, X. Liu, X. Liu and Z. Liu, *Front. Bioeng. Biotechnol.*, 2022, **10**, 1031986.
3 X. Feng, H. Ma, D. Li, G. Sun, T. Zhang, Y. Cui and X. Liu, *Spectrochim. Acta, Part A*, 2025, 127098.
4 X. Yan, D. Lin, D. Yan, D. Wang and H. Su, *Sci. China: Chem.*, 2024, **67**, 2864–2889.
5 J. Zhou, Z. Bao, H. Zhang, Q. Hao, M. Yang, Y. Song and Y. J. Dong, *J. Fluoresc.*, 2025, 1–14.
6 C. C. Wang, S. Y. Ke, C. W. Cheng, Y. W. Wang, H. S. Chiu, Y. C. Ko and G. H. Lee, *Polymers*, 2017, **644**, 9–12.
7 S. Gulati, A. Choudhury, G. Mohan, R. Katiyar, M. A. K. M P, S. Kumar and R. S. Varma, *J. Mater. Chem. B*, 2023, **11**, 6782–6801.
8 B. D. Karuppasamy, S. Perumal, R. Atchudan, A. K. Sundramoorthy, S. Ramalingam, D. Manoj and S. W. Lee, *Inorg. Chem. Commun.*, 2025, 115350.
9 P. Pham, S. Oliver, E. H. Wong and C. Boyer, *Polymer*, 2021, **12**, 5689–5703.
10 O. F. Al Sharif, L. M. Nhari, R. M. El-Shishtawy and A. M. Asiri, *Mater. Today Chem.*, 2023, **29**, 101453.
11 Y. L. Wang, A. Laaksonen and M. D. Fayer, *J. Phys. Chem. B*, 2017, **121**, 7173–7179.
12 O. V. Dolomanov, L. J. Bourhis, R. J. Gildea, J. A. K. Howard and H. Puschmann, *J. Appl. Crystallogr.*, 2009, **42**, 339–341.
13 G. M. Sheldrick, *Acta Crystallogr., Sect. C: Struct. Chem.*, 2015, **71**, 3–14.
14 J. Huang, Y. Chen, P. Zhao, Y. Yu, S. Zhang and Z. Gu, *Regener. Biomater.*, 2018, **5**, 275–282.
15 W.-Q. Zuo, Y.-J. Hu, Y. Yang, X.-Y. Zhao, Y.-Y. Zhang, W. Kong and W.-J. Kong, *J. Neuroinflammation*, 2015, **12**, 105.
16 L. L. Qu, L. He, X. Zhao and W. Xu, *Int. J. Mol. Med.*, 2015, **35**, 1266–1272.
17 W. Cai, J. L. Trefs, T. Hugel and B. N. Balzer, *ACS Mater. Lett.*, 2022, **5**, 172–179.
18 Y. Zhoujin, X. Yang, M. Zhang, J. Guo, S. Parkin and S. Long, *Cryst. Growth Des.*, 2021, **21**, 6155–6165.
19 Q. Chen, A. Afugu, Y. Shuku, Z. F. Liu, K. Awaga and Z. Zhang, *J. Am. Chem. Soc.*, 2025, **147**, 28215–28225.
20 D. Asgari, J. Grüneberg, Y. Luo, H. Küçükkeçeci, S. Ghosh and A. Thomas, *Nat. Commun.*, 2024, **15**, 7031.
21 C. Qin, D. Sun, W. Chen and Z. Chai, *Appl. Math. Model.*, 2025, 116574.
22 R. Svoboda, *Molecules*, 2025, **30**, 175.
23 A. Szlapa-Kula, M. Małecka, A. Maroń, M. Janeczek, M. Schab-Balcerzak and B. Machura, *Inorg. Chem.*, 2021, **60**, 18726–18738.
24 J. R. McLay, J. J. Sutton, G. E. Shillito, C. B. Larsen, G. S. Huff, N. T. Lucas and K. C. Gordon, *Inorg. Chem.*, 2020, **60**, 130–139.
25 D. G. Cai, S. Pan, T. F. Zheng, C. Cao, Z. B. Hu, Y. Peng and S. J. Liu, *Anal. Chem.*, 2026, **98**, 5205–5213.
26 K. Wang, Y. L. Zhu, T. F. Zheng, X. Xie, J. L. Chen, Y. Q. Wu and H. R. Wen, *Anal. Chem.*, 2023, **95**, 4992–4999.
27 İ. Sıdır, Y. G. Sıdır, H. Berber and R. Fausto, *J. Mol. Struct.*, 2023, **1292**, 136191.
28 Y. Zhao, G. Hu, Z. Li, Y. Nie, Y. Li and Y. Zhou, *Microchim. Acta*, 2024, **191**, 606.
29 O. V. Dolomanoy and L. Bourhis, *Appl. Crystallogr.*, 2009, **42**, 339–341.
30 R. K. Sharma and J. K. Bhardwaj, *Biol. Trace Elem. Res.*, 2011, **140**, 291–298.
31 C. Gerner, J. Gotzmann, U. Fröhwein, C. Schamberger, A. Ellinger and G. Sauermann, *Cell Death Differ.*, 2002, **9**, 671–681.
32 N. Droin, C. Rébé, F. Bichat, A. Hammann, R. Bertrand and E. Solary, *Oncogene*, 2001, **20**, 260–269.
33 Z. P. Rokop, W. Zhang, N. Ghosh, N. Biswas, A. Das, J. Lin and C. Kubal, *Surgery*, 2024, **175**, 1539–1546.
34 D. Zhao, C. Liang, J. Qian and J. Shen, *Sci. China: Chem.*, 2025, 1–13.
35 S. Lu, X. Wang, C. He, L. Wang, S. P. Liang, C. C. Wang and P. F. Ge, *Acta Pharmacol. Sin.*, 2021, **42**, 1690–1702.
36 H. Kuang, X. Sun, Y. Liu, M. Tang, Y. Wei, Y. Shi and F. Zhou, *FEBS J.*, 2023, **290**, 3664–3687.
37 M. Park, Y. Jeong, H. S. Kim, W. Lee, S. H. Nam, S. Lee and S. Jeon, *Adv. Funct. Mater.*, 2021, **31**, 2102741.
38 G. Karlström, R. Lindh, P.-Å. Malmqvist, *et al.*, *Comput. Mater. Sci.*, 2003, **28**, 222–239.
39 R. Singh, U. P. Singh, P. Verma, S. Kashyap, R. J. Butcher, C. Ghosh and P. Roy, *CrystEngComm*, 2025, **27**, 5714–5734.

40 T. Verma, U. P. Singh, P. Verma, R. J. Butcher, C. Ghosh and P. Roy, *J. Mol. Struct.*, 2024, **1302**, 137467.
41 P. Verma, *Inorg. Chem. Commun.*, 2024, **170**, 113298.
42 Y. Xie, Q. Chen, M. Wang, W. Chen, Z. Quan and C. Li, *J. Rare Earths*, 2021, **39**, 1467–1476.
43 H. Guo, W. W. Li, M. Y. Wu, J. B. Hu, J. Wang, Y. Liu and K. L. Zheng, *Chin. Chem. Lett.*, 2025, 111721.
44 G. R. Han, O. kwon, S. Kim, J. Choi, J. B. Son, K. S. Min, J. W. Lee, B. Choi and S. K. Kim, *J. Phys. Chem. A*, 2024, **128**, 6124–6131.
45 J. Huang, J. J. Wang, C. Cao, L. Cao, T. F. Zheng, H. R. Wen and S. J. Liu, *Inorg. Chem.*, 2025, **64**, 1551–1560.
46 J. Huang, Z. Y. Li, S. Pan, T. F. Zheng, Y. Wu, H. R. Wen and S. J. Liu, *Inorg. Chem.*, 2026, **65**, 4140–4148.
47 L. Liu, F. Zhang, L. Xu, M. Zhou, B. Yin, T. Tanaka and J. Song, *Chem.–Eur. J.*, 2023, **29**, 202203517.
48 P. Li, D. Shimoyama, N. Zhang, Y. Jia, G. Hu, C. Li and P. Chen, *Angew. Chem., Int. Ed.*, 2022, **61**, 202200612.
49 H. Heng, P. Xu, Z. Wang, X. Ou, J. Chen, Y. Chen and F. Feng, *Chin. Chem. Lett.*, 2025, 112316.
50 (*a*) CCDC 2455666: Experimental Crystal Structure Determination, 2026, DOI: 10.5517/ccdc.csd.cc2nfb1h; (*b*) CCDC 2455667: Experimental Crystal Structure Determination, 2026, DOI: 10.5517/ccdc.csd.cc2nfb2j.